

Microelectrode for energy and current control of nanotip field electron emitters

S. Lüneburg, M. Müller, A. Paarmann, and R. Ernstorfer

Citation: *Appl. Phys. Lett.* **103**, 213506 (2013); doi: 10.1063/1.4831735

View online: <http://dx.doi.org/10.1063/1.4831735>

View Table of Contents: <http://apl.aip.org/resource/1/APPLAB/v103/i21>

Published by the AIP Publishing LLC.

Additional information on Appl. Phys. Lett.

Journal Homepage: <http://apl.aip.org/>

Journal Information: http://apl.aip.org/about/about_the_journal

Top downloads: http://apl.aip.org/features/most_downloaded

Information for Authors: <http://apl.aip.org/authors>



Goodfellow

metals • ceramics • polymers
composites • compounds • glasses

Save 5% • Buy online

70,000 products • Fast shipping

www.goodfellowusa.com

Microelectrode for energy and current control of nanotip field electron emitters

S. Lüneburg, M. Müller,^{a)} A. Paarmann,^{b)} and R. Ernstorfer

Fritz-Haber-Institut der Max-Planck-Gesellschaft, Faradayweg 4-6, 14195 Berlin, Germany

(Received 1 October 2013; accepted 30 October 2013; published online 20 November 2013)

Emerging experiments and applications in electron microscopy, holography, and diffraction benefit from miniaturized electron guns for compact experimental setups. We present a highly compact microelectrode integrated field emitter that consists of a tungsten nanotip coated with a few micrometers thick polyimide film followed by a several nanometers thick gold film, both positioned behind the exposed emitter apex by approximately 10–30 μm . The control of the electric field strength at the nanometer scale tip apex allows suppression, extraction, and energy tuning of field-emitted electrons. The performance of the microelectrode is demonstrated experimentally and supported by numerical simulations. © 2013 AIP Publishing LLC. [<http://dx.doi.org/10.1063/1.4831735>]

Field electron emitters are employed in a wide range of industrial and scientific applications like electron microscopy,¹ electron beam lithography,² and terahertz-sources.³ A continuous miniaturization of electron optics and sources resulted in new types of micrometer-sized lenses,⁴ gated field emitter arrays,⁵ and electron beam microcolumns⁶ that reduce the dimensions of electron sources and optics down to the sub-100 μm range.

More recently, there is an emerging interest in nanotip field emitters as quasi-point-like, yet bright electron source of coherent electron wave packets⁷ for low-energy electron point source (LEEPS) microscopy,⁸ holography,^{9,10} and as laser-triggered source of coherent femtosecond low-energy (single-) electron wave packets for time-resolved diffraction and imaging.^{11–15} Aiming for a time resolution in the sub-picosecond regime, these applications require minimized source-sample distances in order to reduce the effects of temporal broadening during propagation.¹⁵ At the same time, and in particular for diffraction, the use of electron optics is inevitably necessary due to the large intrinsic beam divergence of the electron point source. According to the Fowler-Nordheim theory,¹⁶ the field emission current depends on the electric field which is geometrically enhanced depending on the given size of the emitter and controlled by the applied tip voltage that simultaneously determines the final electron energy. In order to decouple the electron energy and current, electron microscopes (SEM, TEM) utilize a sequence of accelerating, extracting or suppressing electrodes. The latter, generally called suppressor cap, is a bulky electrode pressed on the shaft.¹⁷

In this Letter, we report on the realization of a very compact design of a suppressor-type microelectrode (ME) placed directly onto the shaft of a field emitter, taking the development of miniaturized electron guns one step further. Application of a ME voltage U_{ME} allows to control the field strength at the apex F_{Apex} independently of the acceleration voltage U_{Tip} , thus enables energy and current control of field-emitted electrons at the same time without the need of any post-acceleration. A more positively (negatively) biased

ME, $U_{\text{ME}} > (<) U_{\text{Tip}}$, increases (reduces) F_{Apex} and, thus, the current, while leaving the electron energy constant. This emission control with a miniaturized electrode behind the emitter will be important for applications with μm -scale emitter-sample distances, for instance point projection imaging and holography.^{8,9} Most of these studies employ bare field emitters such that small variations in the tip-sample distance, tip bias, or tip shape and size result in very large changes in the current, easily leading to either loss of image contrast or rapid sample damage. On the other hand, large and distant electrodes become inefficient in controlling the apex field at these small emitter-sample distances. Here, active current control with the presented microelectrode would allow free variation of the electron energy and magnification without loss of contrast and sample degradation.

The design of the field emitter and integrated ME is schematically shown in Fig. 1(a). The core tungsten nanotip is insulated by a few μm thick film of polyimide (PI), leaving the first 10–25 μm of the apex exposed. The PI film is poly[4,4'-oxydiphenylenepyromellitimide] (PMDA-ODA), commonly known as Kapton, which is very suitable as electrical insulator for electron optics in an UHV environment due to its high dielectric strength, high electric resistivity, low outgasing rate, and, especially important for our purposes, its possibility to perfectly adapt to the shape of the tip to ensure the most compact design. The outer gold film acts as ME with a thickness of several nanometers evaporated onto the PI layer and a ME-apex distance of $dz_{\text{ME}} \approx 15 - 30 \mu\text{m}$. Coating the ME directly onto the tip provides a convenient transfer and installation in the vacuum chamber and makes subsequent alignment redundant. In addition, the extremely compact and offset ME allows the apex to be irradiated by strongly focused laser pulses without clipping parts of the beam, even at very small tip-sample distances, as required for time-resolved diffraction or imaging experiments.¹⁵ Furthermore, the absence of large electrodes allows for detection of back-scattered electrons, as envisioned for an ultrafast surface-sensitive LEED experiment in a compact reflective geometry.

The complete fabrication procedure, depicted in Fig. 2(a), is easy to implement, cost-efficient and does not require sophisticated equipment such as focused ion beam (FIB)

^{a)}Electronic mail: m.mueller@fhi-berlin.mpg.de

^{b)}Electronic mail: alexander.paarmann@fhi-berlin.mpg.de

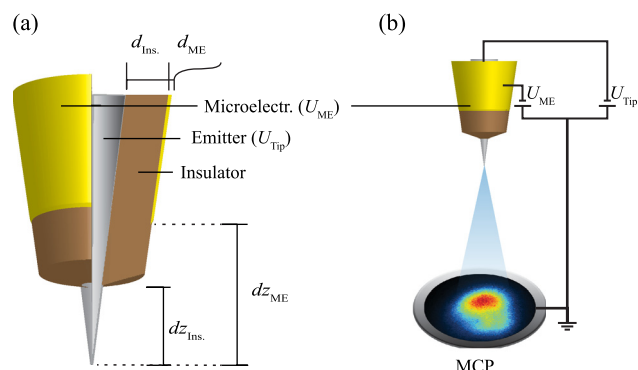


FIG. 1. Schematic representation of the compact ME field emitter (a) and experimental setup (b). A tungsten nanotip is coated by an insulating PI film leaving the apex exposed. The offset between apex and PI film is on the order of $d_{\text{zins}} \approx 10 - 25 \mu\text{m}$, and the film thickness is $d_{\text{ins}} \approx 1 - 3 \mu\text{m}$. The actual microelectrode is coated onto the PI with a distance between apex and ME of $d_{\text{zME}} \approx 15 - 30 \mu\text{m}$ and a thickness of $d_{\text{ME}} \approx 20 - 100 \text{ nm}$. Different voltages U_{Tip} and U_{ME} can be applied to the tip and ME, while the field-emitted electrons are detected on a MCP ≈ 10 cm below the tip.

lithography.⁵ Moreover, the process of coating a nanotip with a PI film is yet unreported and therefore complements to a range of methods that insulate a sharp tip while leaving the apex exposed, as commonly applied in electrochemical scanning tunneling microscopy.^{18–20}

The nanotips are electrochemically etched from $125 \mu\text{m}$ polycrystalline tungsten wire in aqueous 1.5 M KOH using the drop-off method^{21,22} which yields conical tip radii of $20 - 50 \text{ nm}$. Prior to any film coating and gold deposition, the tip apex is protected by a droplet of Apiezon wax W.²³ This is done by carefully dipping the tip into the molten wax at $130 - 140^\circ\text{C}$ using a μm -precision stage and microscope camera. The Apiezon wax meets several requirements essential to the desired design parameters and subsequent fabrication steps: It is insoluble in the polar coating emulsion used for the PI coating, non-invasive to the sharp and sensitive apex,

easy to remove by chloroform (CHCl_3) without distorting the apex, and inherently stable at pressures down to 10^{-6} millibars and thermal radiation in the metal evaporation chamber. Furthermore, the wax dipping allows a radially symmetric apex protection to minimize geometrical aberration and the droplets can be made small enough to cover only a few micrometers of the apex, see Fig. 2(b).

The PI film is afforded by thermal imidization of its precursor poly(amic acid) (PAA) that is electrochemically deposited onto the wire.^{24,25} The emulsion containing the electrophoretic salt of PAA is prepared in three steps: First, 1.1 g of PAA ($12.8 \pm 0.5 \text{ wt. \%}$ solid content, Sigma-Aldrich) containing N-Methyl-2-pyrrolidone (80% NMP/20% aromatic hydrocarbon) is diluted with 5.8 ml dimethylsulfoxide (DMSO) and warmed up to 40°C . Second, 0.20 ml triethylamine (NEt_3) are dripped to the moderately stirred solution and let to react for 20 min . The solution containing the poly(amic acid) amine salt is cooled to room temperature and poured into 17.1 ml of acetone under vigorous stirring. This yields a milky colored colloidal emulsion with a solid content of 0.67 wt. \% , a precipitator/solvent volume ratio of 2.5 and a NEt_3/COOH molar ratio of 2.1 .²⁵ The PAA is deposited from the emulsion by applying a potential of $15 - 20 \text{ V}$ to the tip for 1 min , see Fig. 2(c). A tungsten coil is used as counterelectrode. Since this is a self-limiting deposition process, the final film thickness depends on the deposition potential and composition of the emulsion.^{25,26} The electrochemical deposition results in a radially constant film thickness, hence minimized aberration effects. The uncoated wax droplet is removed by rinsing the apex with CHCl_3 . Afterwards, the tip is heated in a first step to 190°C for 45 min to drive the imidization with a high solvent, i.e., plasticizer, content,^{27–29} and finally, the temperature is raised to 350°C to remove any residual solvents,



This procedure yields PI film thicknesses in the range of $1 - 3 \mu\text{m}$. Subsequently, the apex and few micrometers of PI are wax-protected again to coat the tip with a thin layer of gold by metal vapor deposition in an evaporation chamber at a pressure of $1 \cdot 10^{-6}$ millibars. In the first step, a few nanometers of chromium are deposited serving as wetting agent between the polyimide and gold.³⁰ Without exposure to air, a layer of 50 nm gold is evaporated onto the wires. Using chromium is expected to improve the adhesion, but we observe that gold directly coated on PI is also sufficiently adhesive. To obtain a radially symmetric gold thickness, the wires are mounted perpendicular to the vapor flow and rotated during the deposition process. After the metal deposition, the metal coated wax droplet exhibits cracks due to the heating in vacuum during the evaporation, and thus can be again easily removed by rinsing with CHCl_3 . A typical ME resulting from this process is shown in the SEM image in Fig. 2(d).

The insulation properties of the PI film are essential for the operation of the ME and depend on the degree of imidization from PAA to PI. Therefore, the films are characterized by attenuated total reflectance infrared spectroscopy (ATR-IR) monitoring the total decay of the amide and a

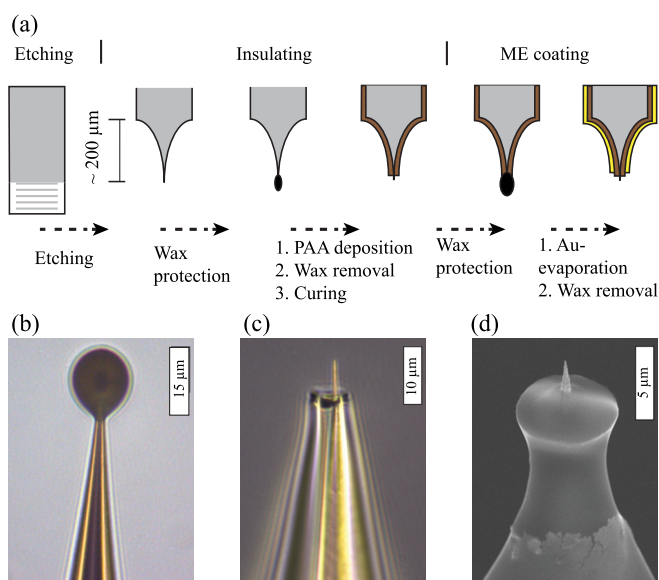


FIG. 2. (a) Schematic process chart of the ME fabrication. (b) Image of the apex protected by an Apiezon wax droplet. (c) Optical microscope image of a tungsten tip coated with PAA and exposed apex after removal of the protecting wax. (d) SEM image of a finished microelectrode: $d_{\text{zins}} \approx 3 \mu\text{m}$, $d_{\text{zME}} \approx 14 \mu\text{m}$, and $d_{\text{ME}} = 50 \text{ nm}$.

strong increase of imide bands after curing indicating a high degree of imidization.^{31,32} The resistance between the tungsten and gold layer exceeds 500 MΩ, and breakthrough voltages of >1000 V are observed, corresponding to a dielectric strength >300 V/μm which is typical for PI.³³

The operation of the ME is tested by analyzing the field emission current as a function of the ME voltage U_{ME} for various tip voltages U_{Tip} experimentally and theoretically, see Fig. 3. Generally, the Fowler-Nordheim (FN) theory allows to calculate the emission current density J as a function of the electric field F_{Apex} at the field emitter apex¹⁶

$$J = aF_{Apex}^2 \exp\left(-\frac{b}{F_{Apex}}\right), \quad (1)$$

where a and b can usually be assumed constant. For an uncoated field emitter, F_{Apex} is often approximated as $F_{Apex}^0(U_{Tip}) = U_{Tip}/kr$, where r is the apex radius and k is the geometrical field enhancement factor.¹⁶ By superposition, the ME contributes an additional electric field which is equally geometrically enhanced in the vicinity of the apex, such that the total field at the apex can be well approximated as

$$F_{Apex} \approx F_{Apex}^0(U_{Tip}) + s(U_{ME} - U_{Tip}), \quad (2)$$

where s is a positive, tip/ME geometry dependent parameter that represents the sensitivity of F_{Apex} to the ME voltage. From Eq. (2), it is clear that a cutoff voltage U_{ME}^{Cutoff} exists for any geometry where $F_{Apex} = 0$. For ME voltages smaller, i.e., more negative, than U_{ME}^{Cutoff} , the electric field direction is reversed and field electron emission is completely suppressed. Since F_{Apex} changes linearly with U_{ME} , the

U_{ME} -dependence of J is expected to exhibit the typical FN behavior, although shifted by the cutoff voltage. Current extraction, i.e., increase of the field emission current compared to the equivalent uncoated emitter, is achieved for $U_{ME} > U_{Tip}$, while partial suppression is observed for ME voltages in the range of $U_{ME}^{Cutoff} < U_{ME} < U_{Tip}$.

The experiment schematically shown in Fig. 1(b) is performed under UHV conditions at a pressure of $2 \cdot 10^{-10}$ millibars. The field-emitted electrons are amplified by a microchannel plate (MCP) detector in Chevron configuration and imaged on a phosphor screen by a scientific CMOS camera (Orca Flash 4.0, Hamamatsu). The grounded front plate of the MCP acts as the anode positioned ≈ 10 cm away from the tip. The recorded intensity on the MCP is converted into current using a calibration obtained by single electron event counting in the low current regime. All measurements presented originate from the ME shown in Fig. 3(b). The measured emission current as a function of the ME voltage is shown in Fig. 3(d) for various tip voltages. The $I - U_{ME}$ curves show the expected FN-type behavior, i.e., the current decreases strongly with decreasing U_{ME} at a given tip voltage. In essence, these measurements show that the electron kinetic energy can be varied over a wide range while maintaining a constant current providing full energy and current control.

The observed experimental behavior is also reproduced in simulations where we calculate the field emission current I according to Eq. (1). The geometrical parameters are based on the ME shown in Fig. 3(b). For tungsten, a work function of $\Phi = 4.5$ eV³⁴ and a tip radius of 25 nm is assumed. The electric field is obtained by numerical simulations of the electrostatics around the ME-coated nanotip using a finite element software;³⁵ see Figs. 3(a) and 3(c) for an example of

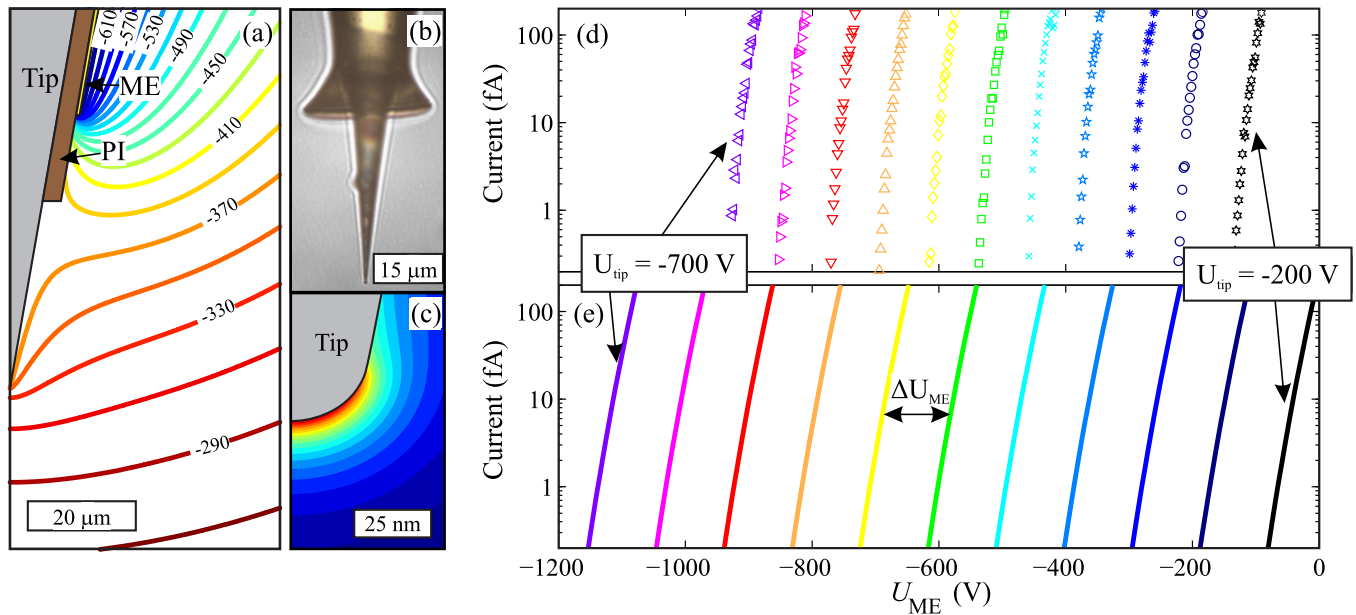


FIG. 3. (a) Electrostatic potential of a nanotip at $U_{Tip} = -400$ V and ME at $U_{ME} \sim -660$ V, resulting in an electric field at the apex of $F_{Apex} = 1$ GV/m. Electrostatic equipotential lines are drawn every 20 V. (b) SEM image of the ME-coated nanotip with a 15 μm scale bar. (c) Color map of the electric field distribution in the vicinity of the apex, illustrating the confined emission area due to the localized field enhancement. The experimental (d) and calculated (e) emission current is plotted on a logarithmic scale as function of the ME voltage U_{ME} for several U_{Tip} from -700 to -200 V in steps of 50 V. The simulation geometry is adapted from the same tip that is also used for the measurements, shown in (b). The experimental and simulated curves agree well in their principal behavior and absolute current values. However, the ME voltage difference ΔU_{ME} separating the $I - U_{ME}$ curves is $\sim 30\%$ larger in the simulations compared to the experiment. Note that the ME acts as extractor when $U_{ME} > U_{Tip}$ and as suppressor when $U_{ME} < U_{Tip}$.

the obtained potential and field distribution at the tip apex, respectively. Notably, the calculated current characteristics shown in Fig. 3(e) reproduce well the absolute values and slopes of the experimental curves.

All U_{Tip} scan curves are separated by a constant ME voltage difference ΔU_{ME} that is inversely proportional to s . The magnitude of ΔU_{ME} is an indication of the effectiveness of the microelectrode, i.e., how much the ME bias needs to be changed in order to compensate a change in U_{Tip} to maintain the same F_{Apex} . Because ΔU_{ME} in the experiment (Fig. 3(d)) is about 30% smaller than in the calculations (Fig. 3(e)), the ME appears to be more effective than the simulations would suggest. However, the simulations have no free parameters other than the tip radius, and largely simplify the complex emission process at the apex, which might lead to the deviation in ΔU_{ME} .

The effectiveness of the ME depends on geometric factors and increases most importantly with a reduced apex-ME distance dz_{ME} and, albeit to a minor extent, with a larger tip opening angle and thicker gold layer. A more effective ME allows for a larger tuning range of the electron energies before dielectric breakdown of the insulation.

Aside from electron suppression (extraction), the ME slightly reduces (increases) the electron beam divergence due to the deformation of the equipotential lines in the entire propagation space. For the data set shown in Fig. 3(d), the beam opening angle increases by $\sim 20\%$ from $U_{\text{Tip}} = -700$ V to $U_{\text{Tip}} = -200$ V when maintaining the same current. Likewise, decreasing U_{ME} at a given tip voltage causes a slight reduction of the beam divergence. This collimation effect becomes significant only for U_{ME} very close the cutoff voltage $U_{\text{ME}}^{\text{Cutoff}}$. In this regime, the ME allows for collimation and focusing of photo-emitted electrons while field electron emission is completely suppressed. Such usage of the microelectrode as a microlens for short electron pulses will be subject of a forthcoming publication.

In conclusion, a nano-sized tungsten field emitter tip has been equipped with a highly compact microelectrode that allows for controlling the current and kinetic energy of field-emitted electrons. The nanotip is surrounded by a 1–3 μm thick polyimide film followed by a 20–100 nm thick gold layer, both positioned approximately 10–30 μm behind the exposed emitter apex. The operation principle is demonstrated under UHV conditions and modeled with numerical calculations. The field emission current and the final kinetic energy of the electrons can be controlled independently by microelectrode and tip voltages U_{ME} and U_{Tip} . The ME can function as current suppressor when $U_{\text{ME}} < U_{\text{Tip}}$ and alternatively as extractor when $U_{\text{ME}} > U_{\text{Tip}}$. The latter mode allows further reduction of the minimal electron energy at a sufficiently high current compared to an uncoated nanotip. Implementation of the self-aligned microelectrode is particularly advantageous for experiments with emitter-sample distances in the micrometer range, e.g., low-energy electron point source microscopy and holography as well as time-resolved low-energy electron imaging and diffraction. In these time-resolved experiments, the small emitter-sample distance ensures high temporal resolution while the offset and tip-adapted microelectrode facilitates laser access to the

tip apex and detection of back-reflected electrons. As will be discussed in a forthcoming publication, the microelectrode is currently utilized as an electron lens to collimate a pulsed laser-triggered electron beam which will be used in ultrafast electron imaging and diffraction experiments.

The authors would like to thank the Department of Inorganic Chemistry at the Fritz Haber Institute for conducting the electron microscopy measurements, as well as the continuous support with analytical measurements and equipment.

- ¹A. V. Crewe, D. N. Eggenberger, J. Wall, and L. M. Welter, *Rev. Sci. Instrum.* **39**, 576 (1968).
- ²H. Kim, S. Ahn, D. Kim, Y. Kim, and S. Ahn, *Microelectron. Eng.* **86**, 2049 (2009).
- ³Y. C. Kim, S. J. Ahn, H. S. Kim, D.-W. Kim, and S. Ahn, *Nucl. Instrum. Methods Phys. Res. A* **654**, 427 (2011).
- ⁴E. Steinwand, J.-N. Longchamp, and H.-W. Fink, *Ultramicroscopy* **110**, 1148 (2010).
- ⁵P. Helfenstien, K. Jefimovs, E. Kirk, C. Escher, H.-W. Fink, and S. Tsujino, *J. Appl. Phys.* **112**, 093307 (2012).
- ⁶T. H. P. Chang, M. Thomson, E. Kratschmer, H. Kim, and M. Yu, *J. Vac. Sci. Technol. B* **14**, 3774 (1996).
- ⁷R. Gomer, *Field Emission and Field Ionization* (Harvard University Press, Cambridge, MA, 1961).
- ⁸M. Germann, T. Latychevskaia, C. Escher, and H.-W. Fink, *Phys. Rev. Lett.* **104**, 095501 (2010).
- ⁹J. Y. Mutus, L. Livadaru, J. T. Robinson, R. Urban, M. H. Salomons, M. Cloutier, and R. A. Wolkow, *New J. Phys.* **13**, 063011 (2011).
- ¹⁰H.-W. Fink, W. Stocker, and S. Heinz, *Phys. Rev. Lett.* **65**, 1204 (1990).
- ¹¹B. Barwick, C. Corder, J. Strohaber, N. Chandler-Smith, C. Uiterwaal, and H. Batelaan, *New J. Phys.* **9**, 142 (2007).
- ¹²H. Yanagisawa, C. Hafner, P. Doná, M. Klöckner, D. Leuenberger, T. Greber, M. Hengsberger, and J. Osterwalder, *Phys. Rev. Lett.* **103**, 257603 (2009).
- ¹³M. Krüger, M. Schenk, and P. Hommelhoff, *Nature* **475**, 78 (2011).
- ¹⁴G. Herink, D. R. Solli, M. Gulde, and C. Ropers, *Nature* **483**, 190 (2012).
- ¹⁵A. Paarmann, M. Gulde, M. Müller, S. Schäfer, S. Schweda, M. Maiti, C. Xu, T. Hohage, F. Schenk, C. Ropers, and R. Ernstorfer, *J. Appl. Phys.* **112**, 113109 (2012).
- ¹⁶R. H. Fowler and L. Nordheim, *Proc. R. Soc. London* **119**, 173 (1928).
- ¹⁷H. S. Kim, M. Yu, E. Kratschmer, B. Hussey, and M. Thomson, *J. Vac. Sci. Technol. B* **13**, 2468 (1995).
- ¹⁸S. N. Thorgaard and P. Bühlmann, *Anal. Chem.* **79**, 9224 (2007).
- ¹⁹M. Tuchband, J. He, S. Huang, and S. Lindsay, *Rev. Sci. Instrum.* **83**, 015102 (2012).
- ²⁰A. Goryu, R. Numano, A. Ikeda, M. Ishida, and T. Kawano, *Nanotechnology* **23**, 415301 (2012).
- ²¹J. P. Ibe, P. P. Bey, S. L. Brandow, R. A. Brizzolara, N. A. Burnham, D. DiLella, K. Lee, C. R. K. Marrian, and R. J. Colton, *J. Vac. Sci. Technol. A* **8**, 3570 (1990).
- ²²G. S. Kelsey, *J. Electrochem. Soc.* **124**, 814 (1977).
- ²³Apiezon, *Wax W-(Technical Data Sheet)* (Apiezon, 2013).
- ²⁴D. C. Phillips, U.S. Patent 4,053,444 (11 October 1977).
- ²⁵Y. Chen and J. O. Iroh, *Polym. Eng. Sci.* **39**, 699 (1999).
- ²⁶W. M. Alvin and L. C. Scala, *J. Appl. Polym. Sci.* **27**, 341 (1982).
- ²⁷M.-J. Brekner and C. Feger, *J. Polym. Sci., Part A: Polym. Chem.* **25**, 2479 (1987).
- ²⁸J.-H. Chang and K. M. Park, *Eur. Polym. J.* **36**, 2185 (2000).
- ²⁹M. Kotera, T. Nishino, and K. Nakamae, *Polymer* **41**, 3615 (2000).
- ³⁰T. Strunskus, M. Grunze, G. Kochendoerfer, and C. Wöll, *Langmuir* **1996**, 2712.
- ³¹Y.-K. Xu, M.-S. Zhan, and K. Wang, *J. Polym. Sci., Part B: Polym. Phys.* **42**, 2490 (2004).
- ³²C. Johnson and S. L. Wunder, *J. Polym. Sci., Part B: Polym. Phys.* **31**, 677 (1993).
- ³³DuPont, *Kapton HN-(Technical Data Sheet)* (DuPont, 2013).
- ³⁴L. Swanson and L. Crouser, *Phys. Rev.* **163**, 622 (1967).
- ³⁵COMSOL Multiphysics 4.2.